

This is a work of the United States Government. In accordance with 17 U.S.C. 105, no copyright protection is available for such works under U.S. Law.

Public Domain Mark 1.0

<https://creativecommons.org/publicdomain/mark/1.0/>

Access to this work was provided by the University of Maryland, Baltimore County (UMBC) ScholarWorks@UMBC digital repository on the Maryland Shared Open Access (MD-SOAR) platform.

Please provide feedback

Please support the ScholarWorks@UMBC repository by emailing scholarworks-group@umbc.edu and telling us what having access to this work means to you and why it's important to you. Thank you.



COSMIC INFRARED BACKGROUND FLUCTUATIONS AND ZODIACAL LIGHT

RICHARD G. ARENDT¹, A. KASHLINSKY², S. H. MOSELEY³, AND J. MATHER³Observational Cosmology Laboratory, Code 665, Goddard Space Flight Center, 8800 Greenbelt Road, Greenbelt, MD 20771, USA; Richard.G.Arendt@nasa.gov, Alexander.Kashlinsky@nasa.gov, Harvey.Moseley@nasa.gov, John.C.Mather@nasa.gov

Received 2016 February 9; accepted 2016 April 14; published 2016 June 7

ABSTRACT

We performed a specific observational test to measure the effect that the zodiacal light can have on measurements of the spatial fluctuations of the near-IR background. Previous estimates of possible fluctuations caused by zodiacal light have often been extrapolated from observations of the thermal emission at longer wavelengths and low angular resolution or from IRAC observations of high-latitude fields where zodiacal light is faint and not strongly varying with time. The new observations analyzed here target the COSMOS field at low ecliptic latitude where the zodiacal light intensity varies by factors of ~ 2 over the range of solar elongations at which the field can be observed. We find that the white-noise component of the spatial power spectrum of the background is correlated with the modeled zodiacal light intensity. Roughly half of the measured white noise is correlated with the zodiacal light, but a more detailed interpretation of the white noise is hampered by systematic uncertainties that are evident in the zodiacal light model. At large angular scales ($\gtrsim 100''$) where excess power above the white noise is observed, we find no correlation of the power with the modeled intensity of the zodiacal light. This test clearly indicates that the large-scale power in the infrared background is not being caused by the zodiacal light.

Key words: cosmology: observations – diffuse radiation – zodiacal dust

1. INTRODUCTION

The study of astronomical backgrounds at various wavelengths allows the examination of sources that are intrinsically diffuse, or individually too faint or too confused to be detected. Over time, improvements in instrumentation may resolve increasingly fainter sources, but very faint and intrinsically diffuse sources always remain in the realm of background studies.

Studies of the cosmic infrared background (CIB) have aimed at measuring the cumulative stellar emission of galaxies across the entire history of the universe. Measurements made by the DIRBE instrument on *COBE* provided the first space-based measurements of the absolute sky surface brightness at wavelengths from 1.25 to 240 μm with an angular resolution of $0.7'$ (Hauser et al. 1998). However, difficulties in accurately removing foreground contributions from the zodiacal light (Kelsall et al. 1998), and from Galactic stars and interstellar dust (Arendt et al. 1998) prevented precise detections of the CIB except at the longest wavelengths.

Subsequent measurements and studies of the CIB at near- to mid-IR wavelengths have made use of telescopes and instruments that provide much higher angular resolution than DIRBE, but which usually cover only a small fraction of the sky, e.g., the Two Micron All Sky Survey, *Spitzer*, *Hubble Space Telescope*, *IRTS*, *AKARI*, *CIBER*. The higher angular resolution allows the exclusion or subtraction of stars and bright galaxies from sky brightness measurements, such that the contribution of Galactic stars is minimized and the remaining CIB does not include the contributions of galaxies brighter than certain limits dependent on the depth of the observations. These data sets are often better suited for measuring the spatial fluctuations or structure of the “source-

subtracted” CIB, rather than for measuring the mean value of the CIB (Kashlinsky et al. 1996a, 1996b, 2002, 2005, 2007a, 2007b, 2012; Kashlinsky & Odenwald 2000; Odenwald et al. 2003; Matsumoto et al. 2005, 2011, 2015; Cooray et al. 2007; Sullivan et al. 2007; Thompson et al. 2007a, 2007b; Arendt et al. 2010; Matsuura et al. 2011; Pyo et al. 2012; Zemcov et al. 2014; Donnerstein 2015; Mitchell-Wynne et al. 2015; Seo et al. 2015). These studies seem to show reasonable consistency of fluctuation measurements reported by different experiments and different groups at $\lambda \gtrsim 2 \mu\text{m}$, though the picture is less clear at shorter wavelengths.

The origin of the fluctuations is not yet clear. The fluctuations may arise from any or all of the following: solar system and Galactic foregrounds, nearby extragalactic contributions, and distant extragalactic contributions. In most cases (e.g., Kashlinsky et al. 2005; Arendt et al. 2010; Matsumoto et al. 2011; Zemcov et al. 2014) foregrounds are estimated by extrapolation of measurements at other wavelengths and locations. This is particularly true of zodiacal light contributions. Mid-IR observations using *ISO* have limited zodiacal light fluctuations to $<0.2\%$ on scales $>3'$ (Abraham et al. 1997). More recent *AKARI* measurements set the limit even lower at 0.03% (Pyo et al. 2012).

Direct detection of zodiacal light influences in *Spitzer* IRAC measurements has been checked in existing deep data sets by constructing $A - B$ difference maps, where A and B represent observations made at two different epochs, typically six months and/or 1 yr apart (e.g., Kashlinsky et al. 2007). The expectation is that the first-order gradient (and any instrumental imprint) should reverse at six-month intervals, while any smaller-scale, physically distinct structures in the interplanetary dust cloud should not remain fixed in a given field (due to differential rotation of the cloud) and should not appear the same at different epochs separated by six months. Excess differences have not been seen in existing deep CIB studies. However, these are generally high-latitude fields where the zodiacal light

¹ CRESST/University of Maryland, Baltimore County.² Science Systems & Applications Inc.³ NASA.

Table 1
COSMOS Zodiacal Light Observations

Epoch	Date	MJD	AOR	Solar Elongation
1	2013 Jan 26	56,318.111	42306048	83.6
2	2013 Feb 02	56,325.130	42306304	90.3
3	2013 Feb 13	56,336.289	42306560	101.0
4	2013 Feb 24	56,347.142	42306816	111.5
5	2013 Mar 02	56,353.211	42307072	117.3

Note. MJD: modified Julian date, AOR: astronomical observation request, Program ID: 80062.

is faint and not strongly modulated. Additionally, at intervals of six months and (especially) 1 yr, the interplanetary dust cloud may be sufficiently symmetric such that certain structures (e.g., those associated with the Earth-resonant ring) may still cancel out in $A - B$ difference maps.

As a more certain test for zodiacal light influences, our new *Spitzer* IRAC observations have monitored a low-latitude field over an entire visibility window to obtain a data set where the zodiacal light is both brightest and most strongly modulated. The observations were planned to be sufficiently deep to detect the reported large-scale background structure. Thus, these data are uniquely suitable for checking whether the zodiacal light intensity has any effect on the reported background fluctuations at large angular scales.

This paper reports on this test and the results. The observations and data reduction are described in Sections 2 and 3. Section 4 provides the characterization of the power spectra of the background. Section 5 discusses the correlations between the various components of the power spectrum and the zodiacal light intensity. Section 6 summarizes the results. Appendix A provides additional detail on temporal variations in the data that are tracked and corrected by the self-calibration procedure that we apply. Appendices B and C feature additional details on the effects of the source model and on the comparison with previous CIB measurements.

2. OBSERVATIONS

Most commonly observed extragalactic fields are chosen because they are at high Galactic and ecliptic latitudes which minimizes the influence of foregrounds. The observations presented here were designed, proposed, and approved specifically for the purpose of examining the effect of zodiacal light on CIB measurements. The COSMOS field (Scoville et al. 2007; Ashby et al. 2013, 2015) is suitable for our experiment, as it lies at relatively low ecliptic latitude. We have selected a subregion at ecliptic coordinates $(\lambda, \beta) = (151.73, -8.63)$ that is relatively free of bright sources. The patch is observed five times across an entire visibility window of the *Spitzer* spacecraft (Werner et al. 2004; Gehrz et al. 2007), covering the widest possible range of solar elongation and thus brightness. The size, $\sim 10' \times 10'$, and depth, ~ 4 hr per epoch, of the patch were chosen to be sufficiently wide and deep to distinguish the large-scale fluctuations above the random white noise in the observations. We use *Spitzer*'s IRAC instrument (Fazio et al. 2004) to collect 3.6 and 4.5 μm data. As IRAC's field of view is $5' \times 5'$, the observations require mosaicking 2×2 fields of view and a total observing time of ~ 16 hr at each epoch. Table 1 lists the dates, solar elongations, and

astronomical observation request (AOR) numbers of the observations.

3. DATA REDUCTION

3.1. Self-calibration

We reduce the data using the same self-calibration techniques (Fixsen et al. 2000) that have been previously employed (Arendt et al. 2010). The data reduction began with the IRAC cBCD individual frames and applied a data model of

$$D^i = S^\alpha + F^p + F^q, \quad (1)$$

where D^i is the measured intensity at pixel i in a single frame (q), S^α is the true sky intensity at location α , F^p is an offset for pixel i that is constant over all frames, and F^q is an offset for frame q that is constant over all pixels (but variable with time). Each of the five epochs is self-calibrated separately to provide detector offsets, F^p , that are appropriate for each epoch. Sky maps are generated on a pixel scale of $0''.6$ (half the size of the detector pixels) using an interlacing algorithm. In addition to regular sky maps, we also create $A - B$ sky maps where all the odd-numbered frames are multiplied by -1 before mosaicking the image. This has the effect of removing the contributions of fixed celestial sources and leaving only instrumental noise (and photon shot noise; see Section 4.1).

Figure 1 shows the 3.6 and 4.5 μm images (S^α determined by self-calibration) of the combined five epochs of observations. The images are cropped to show only the roughly uniformly covered region that was used for power spectrum analysis. Linear background gradients have been fitted and subtracted.

Figure 2 displays the derived values of the detector offsets, F^p , for 3.6 and 4.5 μm at all five epochs. At all epochs there are different patterns of light and dark latent images, which are very slowly decaying imprints of very bright stars as they were dithered across the detector in previous observations. In several cases the tracks of bright stars that slewed across the detector between pointings can also be seen. Residual stray light in the cBCD frames is also revealed and removed by the self-calibration. Diffuse patches of stray light are created by the zodiacal light (and the sum of all other backgrounds) in the upper left and upper right corners of both the 3.6 and 4.5 μm detectors. The BCD pipeline uses estimates of the expected brightness of the zodiacal light to model and remove this stray-light component. These self-calibration results show that at 3.6 μm that process works well initially, when the zodiacal light is bright, but has an increasing error at later epochs as the elongation increases and the zodiacal light becomes fainter. The opposite occurs at 4.5 μm , where the standard correction works best at the later high-elongation epochs and less well at the early epochs when the zodiacal light is brighter. All these features visible in the F^p maps are systematic effects that are removed by the self-calibration of the data.

Figure 3 shows the expected general trend of the zodiacal light intensity as a function of time, as estimated by the *Spitzer* foreground model⁴ and given as the ZODY_EST keyword in the header of each frame. Note that the 4.5 μm intensity is a stronger function of time or elongation than the 3.6 μm intensity, indicating that the color of the zodiacal light is not

⁴ <http://ssc.spitzer.caltech.edu/warmmission/propkit/som/bg/background.pdf>

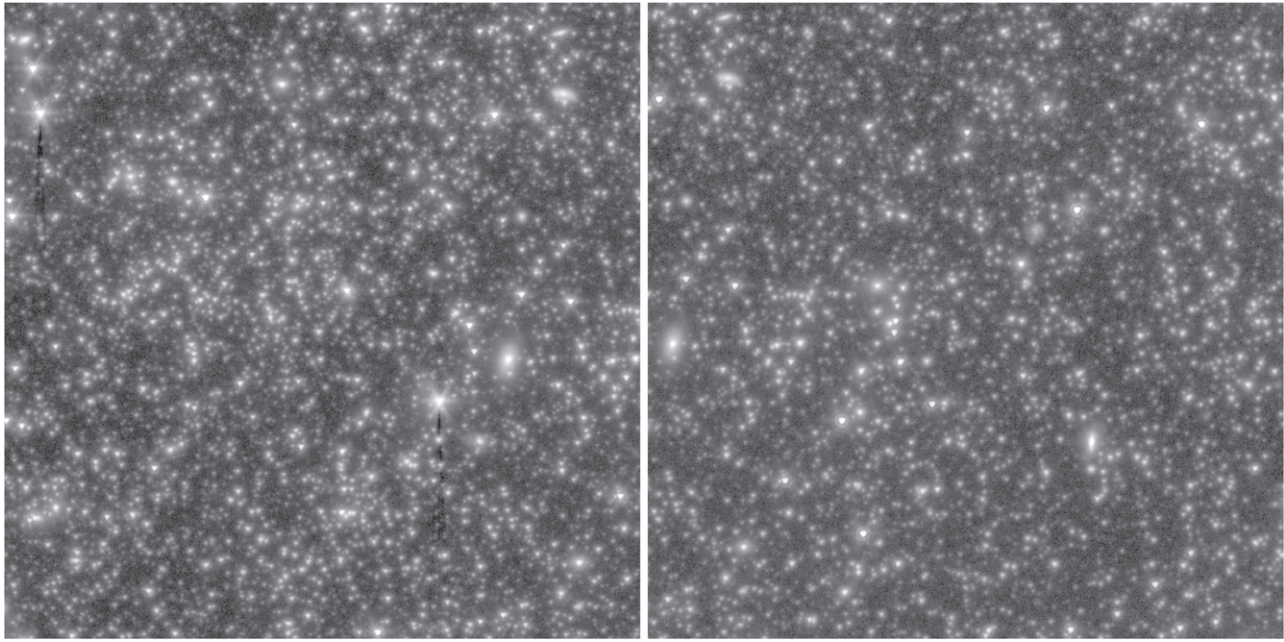


Figure 1. Combined five-epoch $3.6\ \mu\text{m}$ (left) and $4.5\ \mu\text{m}$ (right) mosaics of the study fields, illustrating the source density and the absence of bright stars and large galaxies. Only the two brightest stars in the $3.6\ \mu\text{m}$ image show a small residual of incompletely corrected “column pull-down” artifacts (dark vertical stripes). The images are logarithmically scaled on the range $[2.5 \times 10^{-4}, 1.0]\ \text{MJy sr}^{-1}$ after the addition of an offset of $0.004\ \text{MJy sr}^{-1}$ to avoid logarithmic scaling of negative data values. The images are 900×900 pixels or $9' \times 9'$ in size (1 pixel = $0''.6$). Celestial north is at a position angle of $66^\circ.4$ (counterclockwise from vertical). There is only $\sim 25\%$ overlap between the fields.

expected to be constant. The self-calibration model applied in Equation (1) assumes a fixed sky intensity. Thus, any variations in brightness due to changing zodiacal light intensity across the span of the data being self-calibrated, or a single epoch, are absorbed by the variable offset term, F^q . Figure 4 shows that F^q varies by a much larger amount than the expected zodiacal light trends at $3.6\ \mu\text{m}$, but is similar to the expected zodiacal light trends at $4.5\ \mu\text{m}$. In Appendix A we show that the differences are real and represent corrections for transient instrumental effects (not fully corrected in the BCD pipeline) and residual linear gradients across the field.

3.2. Source Subtraction and Masking

For measurement of the power spectra of the background, resolved sources need to be masked or modeled and subtracted from the images. As in prior studies, we subtract the flux from sources above the noise level using an iterative algorithm described by Arendt et al. (2010). The iterations are halted when the skewness of the intensity distribution of the remaining pixels is zero (independently for each epoch). Because the removal is imperfect, the image is also masked using a mask derived from a surface brightness threshold in the original images for all epochs combined. The masking threshold can equivalently be expressed as a specified surface brightness, a specified maximum outlier in the distribution of surface brightness of unmasked pixels, or a specified fraction of area masked. In this case we chose the last constraint, limiting the masked out regions at both wavelengths to 25% of the image, leaving 75% of the image remaining. At 3.6 and $4.5\ \mu\text{m}$, this limit corresponds to surface brightness thresholds of $\max(I_\nu) - \text{mean}(I_\nu) = 0.0057$ and $0.0044\ \text{MJy sr}^{-1}$ and to maximum outliers of $\max(I_\nu)/\sigma_{I_\nu} = 3.2$ and 2.6 , respectively.

4. POWER SPECTRA

The power spectra of the source-subtracted images are calculated as described by Arendt et al. (2010). The power on the horizontal ($u = 0$) and vertical ($v = 0$) axes in the Fourier domain is omitted when averaging the power in bins at different angular scales, $2\pi/q$. This makes the results less susceptible to certain systematic errors (such as the residual column pull-down seen at $3.6\ \mu\text{m}$ in Figure 1), but limits the maximum angular scale to $382'' = 540''/\sqrt{2}$ instead of the full $540''$ size of the field. The uncertainties assigned to each binned point in the power spectra are the standard deviations of all measurements contributing to each bin. The resulting power spectra, for the five epochs combined and for each epoch individually, are plotted in Figures 5 and 6.

The power spectra are characterized as in Arendt et al. (2010) by fitting a combination of three simple components:

$$P(q) = a_0(2\pi/q/100'')^{a_1} P_{\text{PRF}}(q) + a_2 P_{\text{PRF}}(q) + a_3 \quad (2)$$

where a_0 and a_1 are the amplitude and index of a power-law component that is modulated by the instrument beam or point response function (PRF), $P_{\text{PRF}}(q)$, a_2 is the amplitude of the sky shot noise, a white shot-noise component that is also modulated by the beam (e.g., Poisson variation in the number of faint unresolvable sources in the beam at each location), and a_3 is the amplitude of a white (shot-noise) component that is not modulated by the beam. As an alternate characterization, we also fit

$$P(q) = b_0(2\pi/q/100'')^{b_1} P_{\text{PRF}}(q) + b_2 P_{\text{PRF}}(q) + P_{A-B}(q) \quad (3)$$

where the white-noise component is replaced by the measured $A - B$ power spectrum with no rescaling allowed. These

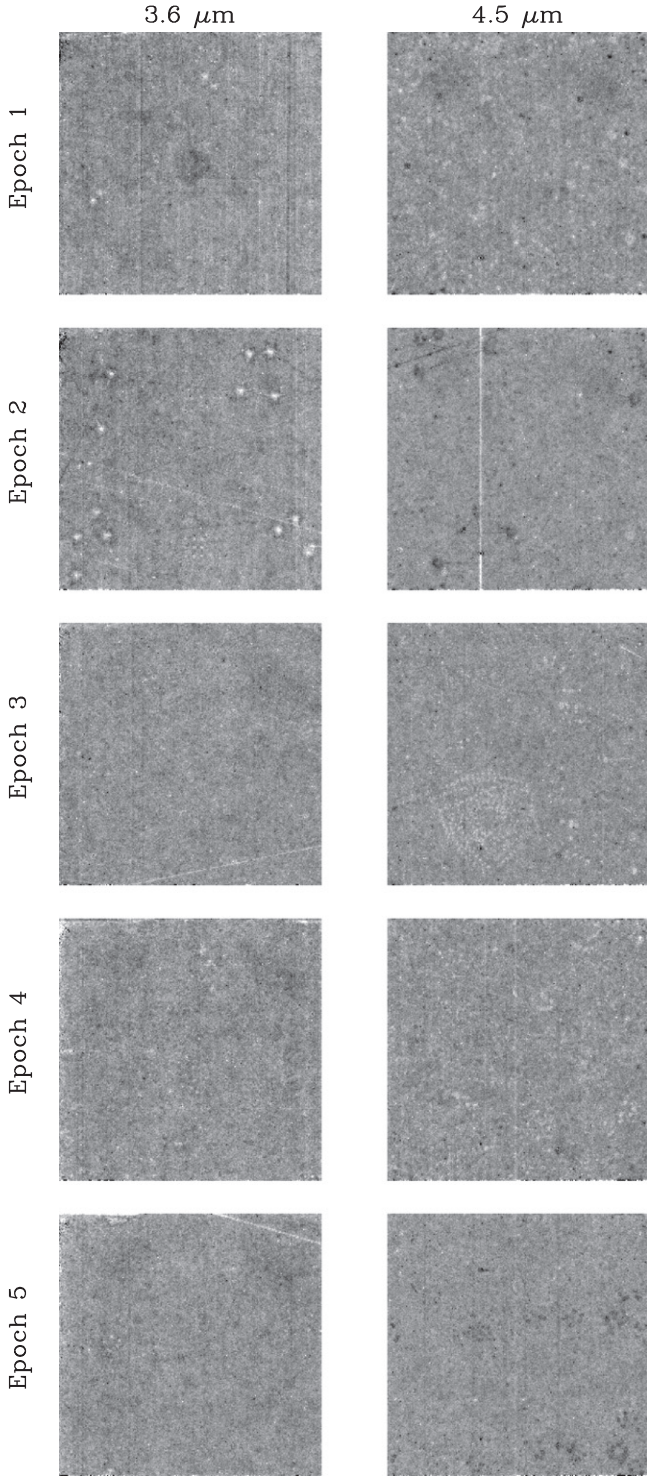


Figure 2. Maps of the self-calibration F^p offsets derived for each epoch. Different long-term latent images are present at each epoch. The effects of residual stray light in the cBCD images are evident as diffuse dark patches in the upper left and right corners of the later epochs at $3.6\ \mu\text{m}$ and the early epochs at $4.5\ \mu\text{m}$. All images are on a linear stretch of $[-0.015, +0.015]\ \text{MJy sr}^{-1}$.

characterizations of the power spectra are overplotted in Figures 5 and 6 and are tabulated in Table 2.

The values of reduced chi squared (χ_ν^2) in Table 2 are calculated for each fit using the full data set, i.e., $\nu = 445$ or 446 degrees of freedom for Equation (2) or Equation (3).

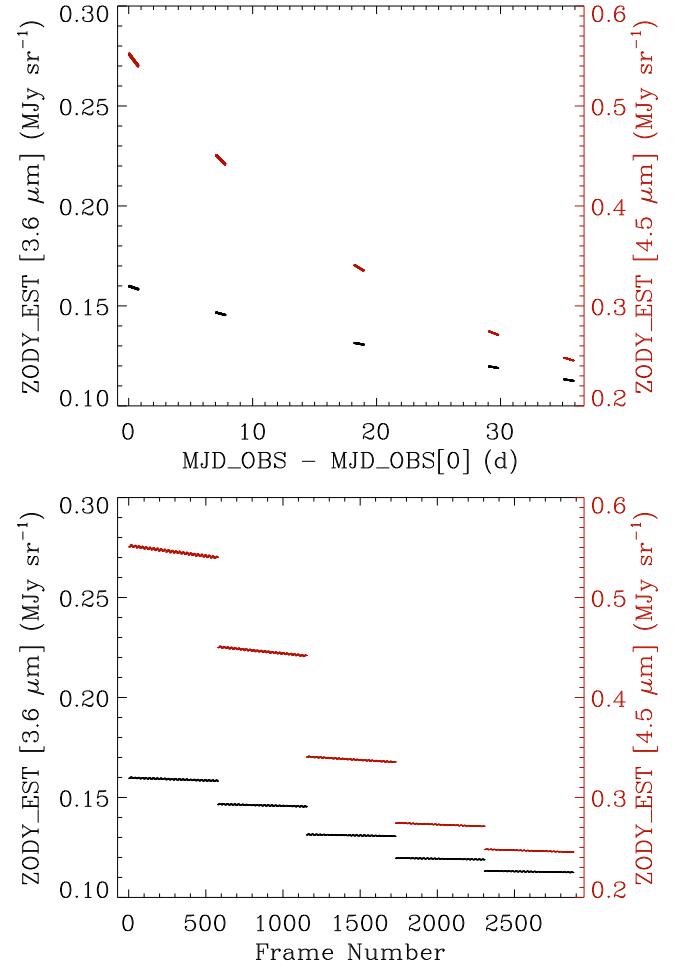


Figure 3. Predicted zodiacal light intensity as given by the ZODY_EST keyword in the cBCD frames. The top plot shows the steady decline in intensity as a function of time. The fractional decrease at $4.5\ \mu\text{m}$ is larger than that at $3.6\ \mu\text{m}$. Plotting simply as a function of frame number (bottom) provides a slightly clearer look at the very small oscillations in intensity that are caused by moving up and down the zodiacal light gradient at different pointings.

However, for the $3.6\ \mu\text{m}$ power spectra, we strongly deweight the two data points at $2\pi/q > 200''$ because the estimated uncertainties are clearly inconsistent with the behavior of these data points. The absolute values of χ_ν^2 are poor, indicating that the uncertainties may be underestimated or these models do not accurately reflect the power spectra. However, the overall aim of these fits is not to validate a particular physical model of the power spectra, but to reduce the power spectra to a small number of parameters that can be easily compared between power spectra (as we do below), and which provide a convenient approximation to the power spectra.

We note that one could apply a more physical model for characterization of the large-scale component of the power spectra, e.g., a ΛCDM template. However, a simple power law provides a sufficient approximation for a wide possibility of origins, given the angular scales ($\lesssim 400''$) and quality of the data analyzed here.

4.1. White-noise Component

The white-noise component of the power spectrum, a_3 in Equation (2), includes instrumental noise, but it also includes

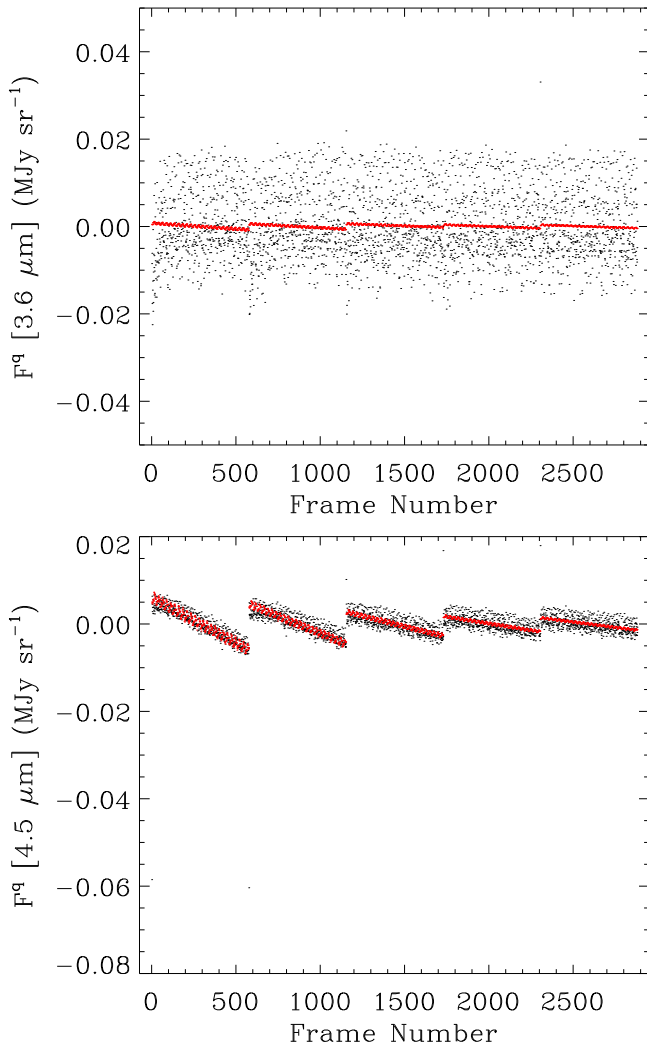


Figure 4. Comparison between the self-calibration F^q offsets (black dots) and the ZODY_EST keyword values (red dots) after subtraction of the mean values for each epoch. The lack of perfect correlation between these reflects errors in the zodiacal light model and the presence of additional temporally variable effects in the data (especially the first-frame effect at $3.6\ \mu\text{m}$; see Appendix A), which are removed by F^q .

the photon shot noise from celestial sources. In particular, the zodiacal light is the dominant brightness component. Because it is an approximately uniform source of emission, the power spectrum of its photon shot noise is not modulated by the beam. As a noise term it also does not cancel out in the construction of the $A - B$ difference images, and therefore the power spectra of those images also include the photon shot noise of the zodiacal light.

The slight rise in the white-noise component at the smallest angular scales is an artifact of mapping the data, sampled on $1''.2$ detector pixels, onto a parallel sky map with $0''.6$ pixels. Given our interlacing mapping algorithm, a slight mismatch in the mean level of any single frame will insert power into the map at the Nyquist frequency of the $0''.6$ pixels of the sky map, i.e., at $1''.2$. The multiplication of the image by a mask then convolves this power in the Fourier domain, spreading it to larger angular scales. Thus, the shape of the turn up at the smallest spatial scales is related to the masking, and the amplitude is related to the size of the frame-to-frame background errors. Mapping on a grid that is not so well

aligned with detector orientation can mitigate the effect somewhat. For example, if the sky map is generated on a grid that is rotated by 45° to the detector orientation, then the white-noise component does appear flat. Because this rise cannot be well fit with flat white noise, more than half the contribution to χ^2_ν comes from $2\pi/q < 2''$.

Figure 7 shows the very strong correlation between the zodiacal light intensity and the measured level of the white-noise power spectrum. Extrapolation to zero intensity of the zodiacal light indicates that white-noise power levels in the absence of zodiacal light would be 5.7×10^{-12} and $5.2 \times 10^{-12}\ \text{nW}^2\ \text{m}^{-4}\ \text{sr}^{-1}$ at 3.6 and $4.5\ \mu\text{m}$, respectively. Comparison with the measured white-noise power (a_3 in Table 2) indicates that photon shot noise of the zodiacal light contributes $\sim 40\%$ – 60% of the amplitude of this component, depending on the epoch of the observations.

4.2. Sky Shot-noise and Power-law Components

The sky shot-noise component, characterized by a_2 or b_2 , is not an essential component for fitting the observed power spectra for the five individual epochs. These observations are so shallow that the flat white-noise component can dominate to sufficiently large scales where the power-law component takes over. At $4.5\ \mu\text{m}$, the best fits are obtained without a sky shot-noise component, though this requires shallower power-law indices, a_1 and b_1 , than previously found (Arendt et al. 2010). This is likely caused by an inability to distinguish separate sky shot-noise and power-law components in these shallow data. Constraining the power-law index to be $a_1 = b_1 = 1.0$ does result in a weak sky shot-noise component that constitutes $\sim 15\%$ of the power at $100''$, but the constraint produces a poorer fit at scales of $\sim 20''$. Results of this constrained fit are listed in the last section of Table 2. At $3.6\ \mu\text{m}$ there is no similar motivation for a constrained fit, as the best fits find nonzero sky shot-noise components (a_2 and b_2) and power-law slopes (a_1 and b_1) that are similar to those previously derived (Arendt et al. 2010). Conversely, omitting the sky shot-noise component (a_2 and b_2) at $3.6\ \mu\text{m}$ causes the power-law component to flatten, to better fit the spectrum at $2\pi/q \lesssim 10''$. For the all-epochs-combined power spectrum, the power law flattens completely ($a_1 \sim 0$ and $b_1 \sim 0$), to become the sky shot-noise component, leaving the rising power at $2\pi/q \gtrsim 10''$ poorly fit.

The amplitudes, a_0 and b_0 , of the power law fitting the large-scale power at $4.5\ \mu\text{m}$ are much lower than at $3.6\ \mu\text{m}$, unlike prior results, where powers were comparable (Arendt et al. 2010). Figure 8 shows no correlation between the amplitude of the power-law component and the intensity of the zodiacal light.

5. DISCUSSION

The correlation between the zodiacal light intensity and the white noise in the power spectra (Figure 7) indicates both a constant component (i.e., the intercept as the zodiacal light intensity goes to 0) and a component that is proportional to the zodiacal light intensity. Instrumental noise terms (e.g., read noise and dark current) and the photon shot noise from the mean intensity of unresolved Galactic and extragalactic backgrounds would contribute to this constant term. In Figure 9 we present a comparison between the measured white-noise power as a function of zodiacal light intensity and the expected noise levels.

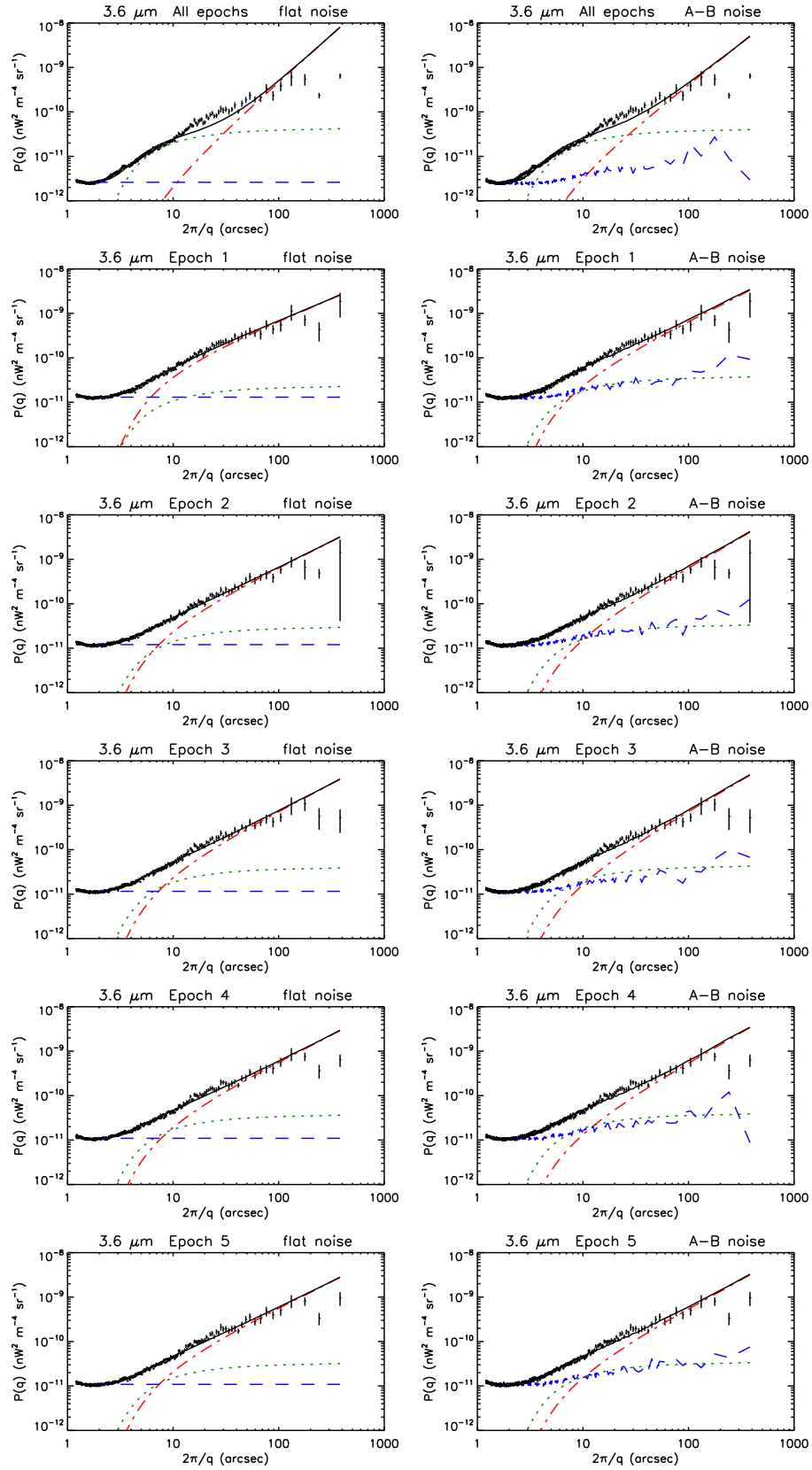


Figure 5. Fits to the $3.6\ \mu\text{m}$ power spectra for all epochs combined and for each of the five separate epochs. The left column shows fits as characterized by Equation (2): (a) flat white-noise components (blue dashed line), (b) a flat shot-noise component convolved with the PRF (green dotted line), and (c) a power-law component, also convolved with the PRF (red dot-dashed line). The black solid line indicates the sum of these three components. The right column shows the fits as characterized by Equation (3), where the measured $(A - B)/2$ noise takes the place of the flat instrument noise component.

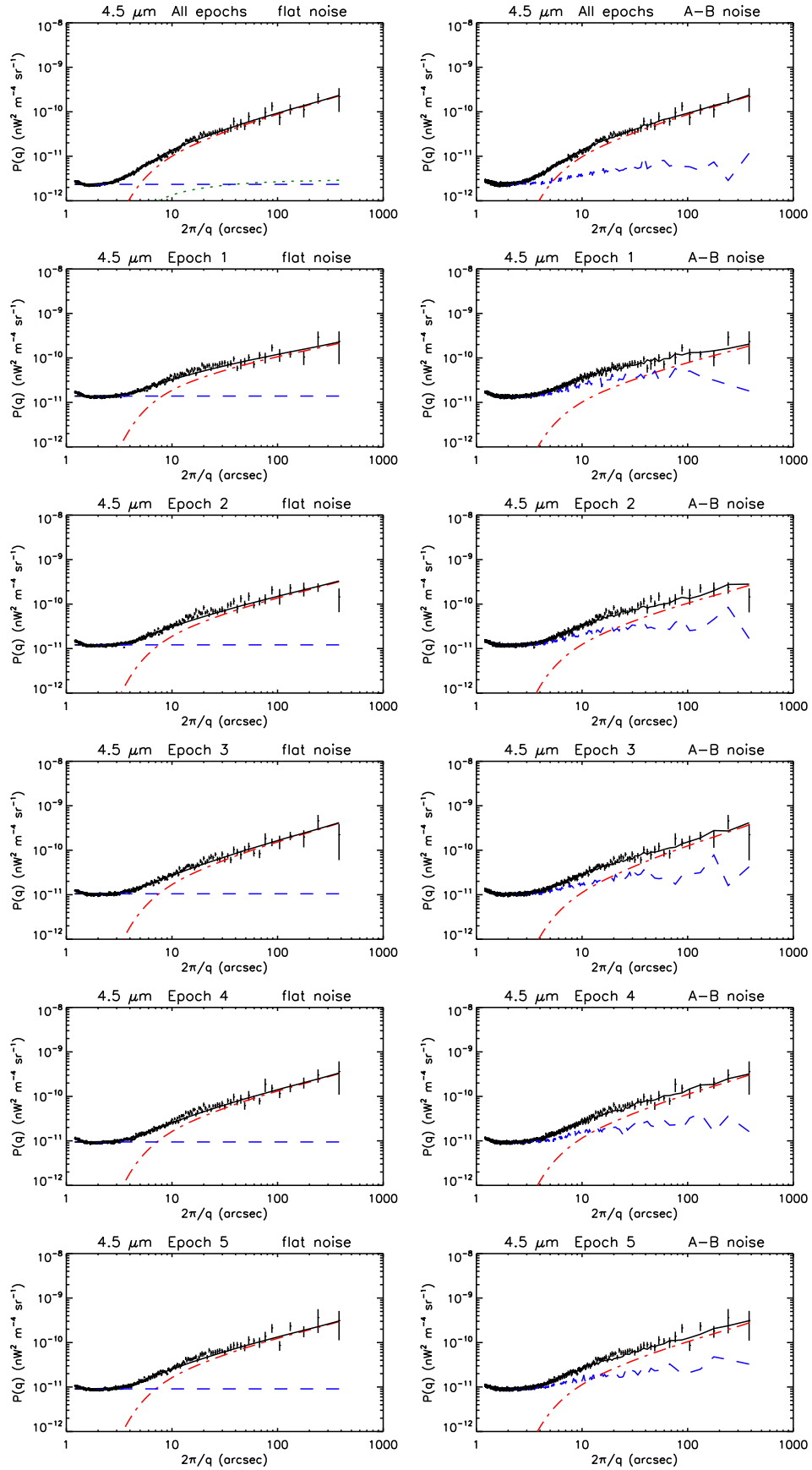


Figure 6. Same as Figure 5, except for $4.5 \mu\text{m}$. Note that a sky shot-noise component is included in all of these fits, but in most cases its preferred amplitude is 0.

Table 2
Power Spectrum Parameters

λ (μm)	Epoch	$10^{11}a_0$	a_1	$10^{11}a_2$	$10^{11}a_3$	χ^2_ν	$10^{11}b_0$	b_1	$10^{11}b_2$	χ^2_ν
3.6	All epochs	50.24 ± 2.82	2.07 ± 0.06	4.19 ± 0.04	0.26 ± 0.001	4.47	43.76 ± 2.90	1.82 ± 0.06	4.01 ± 0.05	5.92
3.6	Epoch 1	70.58 ± 4.23	0.97 ± 0.05	2.26 ± 0.39	1.30 ± 0.003	2.73	70.28 ± 4.65	1.16 ± 0.05	3.73 ± 0.28	2.48
3.6	Epoch 2	68.39 ± 4.21	1.15 ± 0.05	2.95 ± 0.25	1.20 ± 0.002	2.99	68.90 ± 4.60	1.33 ± 0.06	3.33 ± 0.20	2.76
3.6	Epoch 3	77.19 ± 4.73	1.20 ± 0.05	3.89 ± 0.24	1.16 ± 0.002	2.44	77.67 ± 5.09	1.35 ± 0.05	4.26 ± 0.20	2.90
3.6	Epoch 4	60.29 ± 3.60	1.18 ± 0.05	3.63 ± 0.22	1.09 ± 0.002	2.67	58.09 ± 3.75	1.32 ± 0.06	3.86 ± 0.18	2.52
3.6	Epoch 5	60.30 ± 3.65	1.14 ± 0.05	3.20 ± 0.23	1.09 ± 0.002	2.54	58.36 ± 3.82	1.26 ± 0.05	3.36 ± 0.20	3.38
4.5	All epochs	9.61 ± 0.19	0.65 ± 0.02	0.29 ± 0.10	0.23 ± 0.001	3.55	9.44 ± 0.20	0.65 ± 0.02	0.06 ± 0.11	7.25
4.5	Epoch 1	11.59 ± 0.63	0.46 ± 0.04	0.00 ± 0.57	1.39 ± 0.003	5.21	8.50 ± 0.52	0.59 ± 0.06	0.00 ± 0.40	4.56
4.5	Epoch 2	14.94 ± 0.51	0.56 ± 0.03	0.00 ± 0.34	1.21 ± 0.003	5.15	11.38 ± 0.53	0.63 ± 0.04	0.00 ± 0.31	4.51
4.5	Epoch 3	16.76 ± 0.40	0.66 ± 0.03	0.00 ± 0.25	1.05 ± 0.002	4.27	13.62 ± 0.41	0.75 ± 0.04	0.00 ± 0.22	4.24
4.5	Epoch 4	14.37 ± 0.36	0.61 ± 0.03	0.00 ± 0.28	0.95 ± 0.002	4.11	12.11 ± 0.37	0.68 ± 0.04	0.00 ± 0.25	3.57
4.5	Epoch 5	13.52 ± 0.38	0.58 ± 0.03	0.00 ± 0.30	0.91 ± 0.002	3.81	11.36 ± 0.38	0.66 ± 0.04	0.00 ± 0.26	4.29
4.5	All epochs	8.34 ± 0.17	1.0	1.35 ± 0.02	0.23 ± 0.000	3.93	8.15 ± 0.17	1.0	1.09 ± 0.02	7.91
4.5	Epoch 1	7.46 ± 0.19	1.0	2.88 ± 0.06	1.38 ± 0.003	6.03	6.46 ± 0.21	1.0	1.29 ± 0.07	4.81
4.5	Epoch 2	9.22 ± 0.22	1.0	2.57 ± 0.06	1.20 ± 0.002	6.30	7.76 ± 0.24	1.0	1.44 ± 0.07	5.00
4.5	Epoch 3	14.32 ± 0.31	1.0	1.81 ± 0.05	1.04 ± 0.002	4.92	12.24 ± 0.32	1.0	0.87 ± 0.06	4.47
4.5	Epoch 4	12.02 ± 0.24	1.0	1.92 ± 0.05	0.94 ± 0.002	4.82	10.51 ± 0.25	1.0	1.18 ± 0.05	3.91
4.5	Epoch 5	11.09 ± 0.26	1.0	1.99 ± 0.05	0.90 ± 0.002	4.62	9.84 ± 0.26	1.0	1.17 ± 0.05	4.75

Note. Units for a_0 , a_2 , a_3 , b_0 , and b_2 are $\text{nW}^2 \text{m}^{-4} \text{sr}^{-1}$.

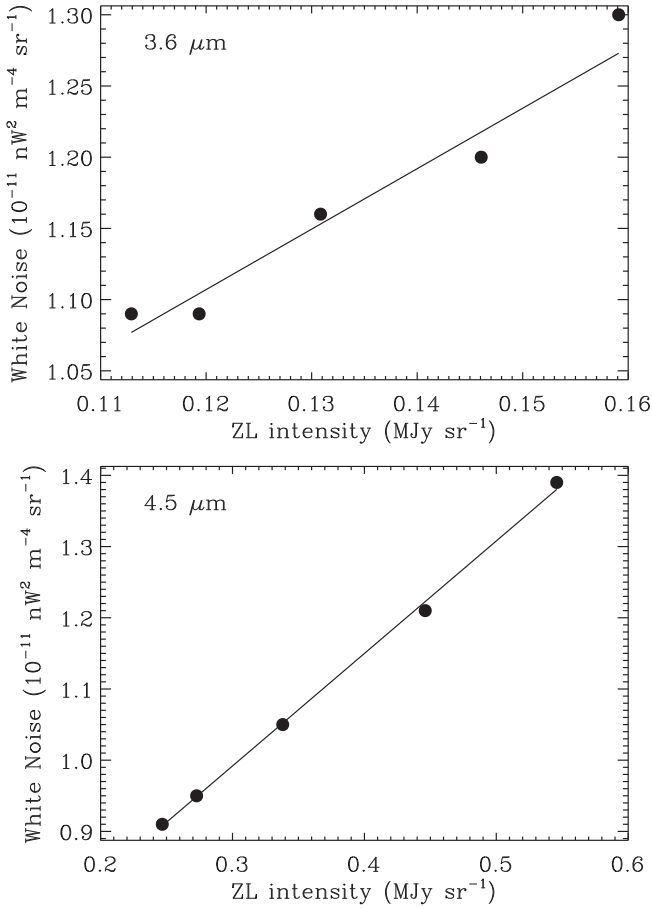


Figure 7. Correlation between the white-noise level (a_3) and the zodiacal light intensity across the five epochs shows that roughly half of the white noise is correlated with the zodiacal light. The formal uncertainties in the white-noise values are smaller than the plotted symbols (see Table 2). The Kendall's τ rank correlations (bounded on the interval $[-1, 1]$) for these quantities at 3.6 and 4.5 μm are 0.95 and 1.0. The probabilities of finding these values of $|\tau|$ (or larger) given uncorrelated data are 0.02 and 0.01.

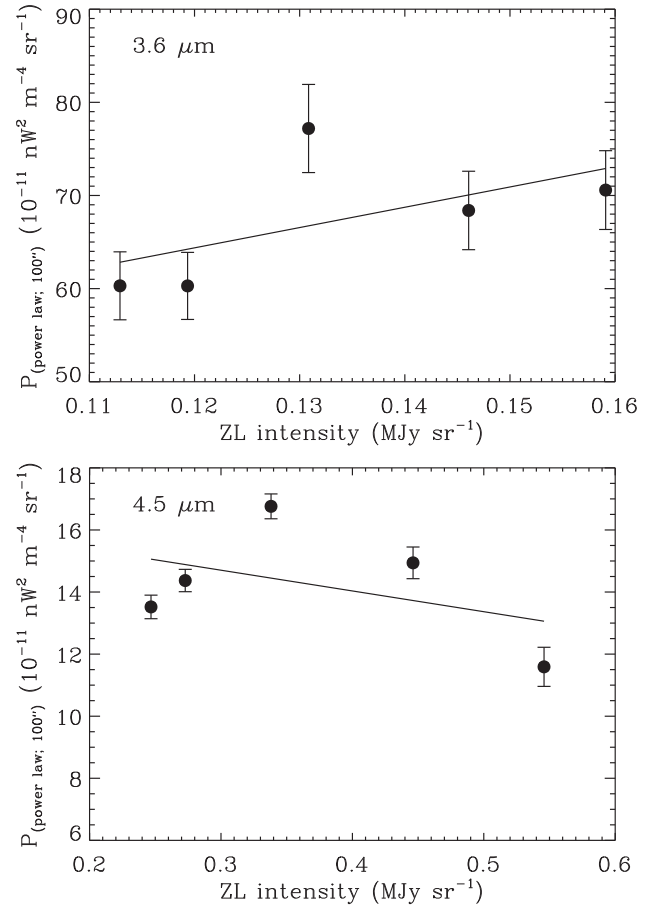


Figure 8. There is no significant correlation between the amplitude of the power-law component (a_0) and the zodiacal light intensity across the five epochs at either 3.6 μm (top) or 4.5 μm (bottom). However, the results shown here are sensitive to the choice of model depth (see Appendix B). The Kendall's τ rank correlations (bounded on the interval $[-1, 1]$) for these quantities at 3.6 and 4.5 μm are 0.4 and 0.0. The probabilities of finding these values of $|\tau|$ (or larger) given uncorrelated data are 0.33 and 1.0.

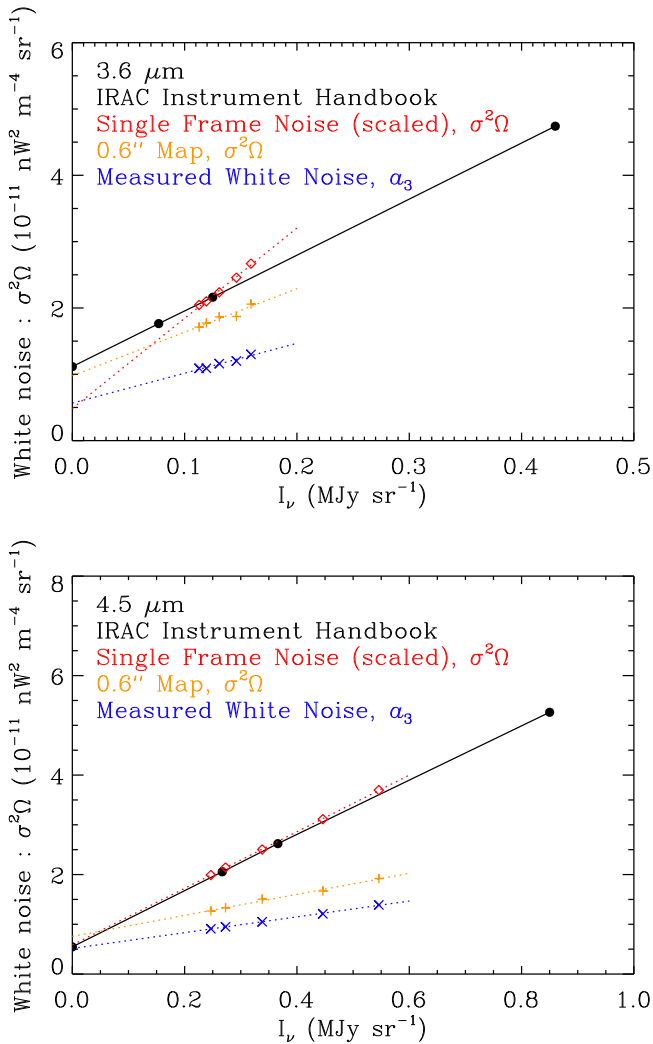


Figure 9. Comparison of white-noise predictions and measurements as a function of background intensity. The expected white-noise levels calculated from the IRAC Instrument Handbook using “High,” “Medium,” and “Low” background levels, and with the background set to 0.0, are shown by the black circles. The mean white-noise levels derived from the measured standard deviation of individual frames at each of the five epochs are shown by red diamonds. The mean white-noise levels derived from the measured standard deviation of the self-calibrated sky maps are shown by orange plus signs. The measured white-noise levels obtained by fits to the power spectra are indicated by the blue crosses. See text for explanation of consistencies and discrepancies.

Using the equations and parameters presented in Section 2.5 of the IRAC Instrument Handbook,⁵ we can evaluate the expected 1σ noise level for extended emission for 100 s frame time exposures during the IRAC warm mission. These numbers are listed in Table 3 (Note 1) and, after conversion to white noise power, $P = \sigma^2\Omega_{\text{pix}}$ (Table 3, Note 5), are shown in Figure 9. For direct comparison to these expected noise estimates, we calculated the mean of the standard deviations of all (576) individual exposures at each epoch. A robust procedure was used to exclude the effect of stars and other statistical outliers. These numbers (Table 3, notes 2 and 6) are in generally good agreement with the expected uncertainties, with the exception that at $3.6\,\mu\text{m}$ the measured standard deviations show more variation with zodiacal light intensity

than expected. This discrepancy may indicate that the zodiacal light model predicts the correct mean intensity of the zodiacal light, but underestimates the modulation of the intensity as a function of time. This effect is very similar to that observed at the north ecliptic pole (NEP) by Krick et al. (2012).

The standard deviation in mosaicked sky maps should be reduced by a factor of $1/\sqrt{N}$, where N is the number of frames contributing at each pixel (Table 3, note 3). In this case there are 144 frames per pointing, but interlaced mapping on $0''.6$ pixels reduces the per pixel coverage by a factor of 4, so $N = 36$. The actual measured standard deviations of the self-calibrated mosaics (Table 3, note 4) are $\sim 10\%$ smaller at $3.6\,\mu\text{m}$ and $\sim 24\%$ smaller at $4.5\,\mu\text{m}$. Converted to a power (Table 3, note 7), these values are plotted as the orange plus signs in Figure 9. They show a similar trend to the white-noise levels derived from the power spectra (a_3 ; blue crosses), but are biased upward because they average the power at all angular scales, rather than just fitting the minimal white noise at the smallest angular scales. The roughly constant size of the bias is a further indication that the large-scale structure is independent of the zodiacal light intensity.

Ideally, the white-noise level extrapolated to a zodiacal light intensity of 0 could be interpreted in terms of instrumental noise plus the photon shot noise from galactic and extragalactic backgrounds. However, systematic errors in the zodiacal light model, as clearly evident at $3.6\,\mu\text{m}$, will directly affect the intercept. This is the likely reason for the mismatch between the extrapolated intercepts for the measured $3.6\,\mu\text{m}$ power (either from the fitted power spectra or from single frames) and the expected noise power as calculated from the IRAC Instrument Handbook. However, the ultimate origin of the white-noise component is not very important for current CIB studies, which normally subtract any “instrumental” or $A - B$ noise term that is constructed to be independent of fixed sources on the sky.

The large-scale component in the source-subtracted CIB power spectrum is the term that is of greatest cosmological interest. Prior studies agree that there is power here in excess of that expected from the faint unresolved galaxies extrapolated from known galaxy populations (Kashlinsky et al. 2005; Sullivan et al. 2007; Cooray et al. 2012; Helgason et al. 2012). The lack of significant correlation between the large-scale power and the zodiacal light intensity (Figure 8) suggests that the zodiacal light is not influencing the large-scale power. Additionally, we note that while the zodiacal light intensity is greater at $4.5\,\mu\text{m}$ than at $3.6\,\mu\text{m}$, the data exhibit weaker large-scale power at the $4.5\,\mu\text{m}$ than at $3.6\,\mu\text{m}$. This also indicates that the zodiacal light is not the main source of the large-scale power.

6. SUMMARY

We performed an experiment specifically designed to measure the impact of the zodiacal light on the estimate of the spatial fluctuations of the CIB. To provide the greatest possible sensitivity to the zodiacal light effect, our test monitored a fixed patch in the COSMOS field at low ecliptic latitude as the mean zodiacal light intensity varied over the full accessible range of brightness (or solar elongation). The CIB spatial power spectrum was calculated at five epochs over this five-week interval. The power spectra are characterized as the sum of (a) a white-noise component, (b) a sky shot-noise component, and (c) a power-law component dominating on large angular scales.

⁵ <http://irsa.ipac.caltech.edu/data/SPITZER/docs/irac/iracinstrumenthandbook/>

Table 3
White-noise Estimates and Measurements

λ (μm)	Quantity	Epoch 1	Epoch 2	Epoch 3	Epoch 4	Epoch 5	$I_A(\text{zodi}) = 0$	Note
3.6	ZODY_EST (MJy sr ⁻¹)	0.159	0.146	0.131	0.119	0.113	0.0	
3.6	σ_{frame} (MJy sr ⁻¹)	0.0119	0.0116	0.0113	0.0110	0.0109	...	1
3.6	σ_{frame} (MJy sr ⁻¹)	0.0124	0.0119	0.0113	0.0110	0.0108	...	2
3.6	σ (MJy sr ⁻¹)	0.00207	0.00198	0.00189	0.00183	0.00181	...	3
3.6	σ (MJy sr ⁻¹)	0.00181	0.00173	0.00173	0.00168	0.00165	...	4
3.6	$\sigma^2\Omega$ (10 ⁻¹¹ nW ² m ⁻⁴ sr ⁻¹)	2.45	2.34	2.21	2.11	2.06	1.12	5
3.6	$\sigma^2\Omega$ (10 ⁻¹¹ nW ² m ⁻⁴ sr ⁻¹)	2.67	2.46	2.24	2.10	2.05	0.48 \pm 0.09	6
3.6	$\sigma^2\Omega$ (10 ⁻¹¹ nW ² m ⁻⁴ sr ⁻¹)	2.06	1.87	1.87	1.77	1.71	0.98 \pm 0.17	7
3.6	a_3 (10 ⁻¹¹ nW ² m ⁻⁴ sr ⁻¹)	1.30	1.20	1.16	1.09	1.09	0.57 \pm 0.07	8
4.5	ZODY_EST (MJy sr ⁻¹)	0.546	0.446	0.338	0.273	0.247	0.0	
4.5	σ_{frame} (MJy sr ⁻¹)	0.0183	0.0169	0.0152	0.0140	0.0135	...	1
4.5	σ_{frame} (MJy sr ⁻¹)	0.0186	0.0171	0.0153	0.0141	0.0136	...	2
4.5	σ (MJy sr ⁻¹)	0.00310	0.00284	0.00255	0.00236	0.00227	...	3
4.5	σ (MJy sr ⁻¹)	0.00223	0.00208	0.00198	0.00186	0.00181	...	4
4.5	$\sigma^2\Omega$ (10 ⁻¹¹ nW ² m ⁻⁴ sr ⁻¹)	3.60	3.06	2.46	2.09	1.94	0.55	5
4.5	$\sigma^2\Omega$ (10 ⁻¹¹ nW ² m ⁻⁴ sr ⁻¹)	3.70	3.11	2.51	2.14	1.99	0.59 \pm 0.01	6
4.5	$\sigma^2\Omega$ (10 ⁻¹¹ nW ² m ⁻⁴ sr ⁻¹)	1.92	1.67	1.51	1.33	1.27	0.76 \pm 0.04	7
4.5	a_3 (10 ⁻¹¹ nW ² m ⁻⁴ sr ⁻¹)	1.39	1.21	1.05	0.95	0.91	0.52 \pm 0.01	8

Notes. (1) Expected extended source surface brightness sensitivity for single 100 s frames as calculated from equations in Section 2.5 of the IRAC Instrument Handbook. (2) Measured average standard deviation (outliers excluded) of single frames. (3) Measured average standard deviation (outliers excluded) of single frames scaled by of $1/\sqrt{N}$. (4) Average standard deviation (outliers excluded) of self-calibrated sky map (0''/6 pixels). (5) White-noise power derived from expected sensitivity (as in note 1). (6) White-noise power derived from standard deviation of single frames. (7) White-noise power derived from standard deviation of sky map. (8) White-noise power derived from fit to power spectrum.

We find that approximately half of the white-noise component is correlated with the varying mean intensity of the zodiacal light. Photon shot noise of the zodiacal light is expected to be the main contribution to this correlated component. Detailed analysis of the non-zodiacal light portion of the white noise is limited by inaccuracies of the zodiacal light model in predicting the intensity in this direction as seen from *Spitzer*'s location within the interplanetary dust cloud.

The sky shot noise in the angular power spectra of the background is not reliably distinguished in the relatively shallow observations of this experiment. The power-law component does not show significant correlation with the mean zodiacal light intensity at 3.6 or 4.5 μm . This confirms that observed spatial fluctuations at large scales ($\gtrsim 100''$) are not being influenced by zodiacal light. Prior observations had been less conclusive because they were usually limited to high ecliptic latitudes, where the zodiacal light is faintest, and to epochs ~ 6 or 12 months apart, where there should be minimal modulations of the zodiacal light intensity.

We thank the referee, M. Zemcov, for comments that improved this paper. Additional helpful comments were provided by M. Ashby. This work is based on observations made with the *Spitzer Space Telescope*, which is operated by the Jet Propulsion Laboratory, California Institute of Technology, under a contract with NASA. This work was funded by JPL under *Spitzer* Cycle 8 funding contract 1464716, and in part through NASA/12-EUCLID11-0003 "LIBRAE: Looking at Infrared Background Radiation Anisotropies with Euclid." This research made use of NASA's Astrophysics Data System Bibliographic Services and the IDL Astronomy Library (Landsman 1993).

Facility: *Spitzer* (IRAC).

Software: IDL.

APPENDIX A TEMPORAL VARIABILITY OF THE IRAC DATA

Figure 4 showed that the temporally variable offset, F^q , derived by the self-calibration is accounting for variations apart from the simple trends expected of the zodiacal light. In this appendix, we demonstrate additional real trends that are being found and subtracted by the F^q term in the self-calibration.

A.1. Zodiacal Light

The main trend expected in F^q is the temporal variation of the zodiacal light as the solar elongation of the target field steadily increases. We model this trend as a constant times the model zodiacal light brightness (as specified by the ZODY_EST keywords in the BCD headers).

A.2. First-frame Effect

Apart from the zodiacal light, the strongest trend in F^q is due to the "first-frame effect" in the IRAC detectors.⁶ This effect appears as a variation in the background level as a function of the time since the previous exposure. It appears most strongly at the first frame in an AOR, when there has been a long slew from the previous target. The BCD pipeline attempts to correct for the first-frame effect, but is not entirely successful. Here we model the first-frame effect as a third-order polynomial function of the delay since the preceding frame (as specified by the FRAMEDLY keywords in the BCD headers).

A.3. Spatial Gradient

The zodiacal light has an intrinsic spatial gradient, being brighter at smaller solar elongations. During the course of

⁶ <http://irsa.ipac.caltech.edu/data/SPITZER/docs/irac/iracinstrumenthandbook/>

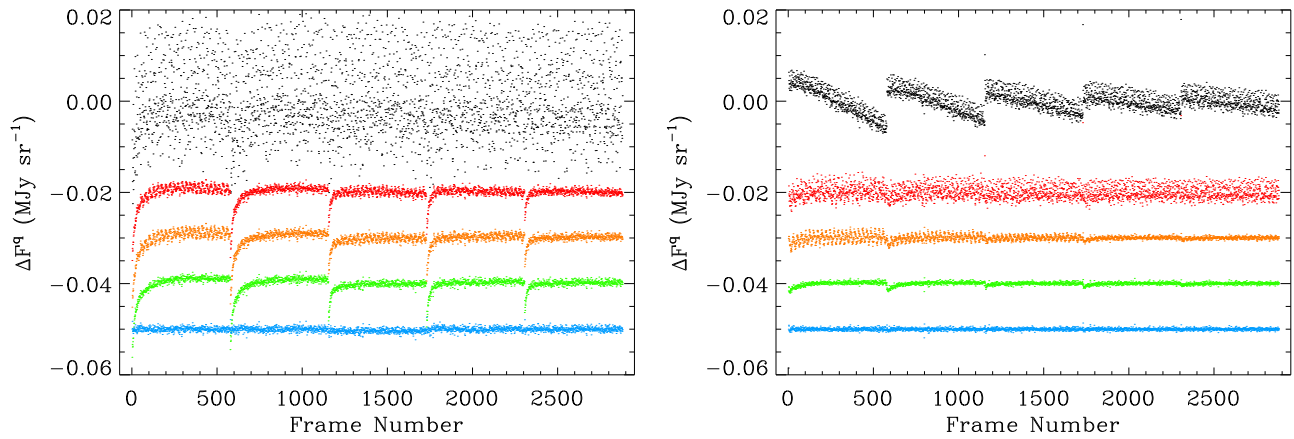


Figure 10. Successive removal of identifiable components of F^q . For $3.6\ \mu\text{m}$ (left) the black dots show the full F^q (as in Figure 4). Each segment of 576 frames corresponds to one AOR. The colored dots show the residual F^q after successive subtraction of decreasingly smaller components: a first-frame effect (red), the zodiacal light variation (orange), an arbitrary linear gradient (green), and an exponential recovery term (blue). At $4.9\ \mu\text{m}$ (right), the relative strength of the components differs and the sequence shown is after successive subtractions of the zodiacal light variation (red), a first-frame effect (orange), an arbitrary linear gradient (green), and an exponential recovery term (blue).

dithering and moving between each of the 2×2 fields of view at each epoch, locations at slightly higher and lower elongations are sampled. The corresponding variations in brightness are thus mapped as temporal variations in F^q . Additionally, the self-calibration is degenerate with respect to linear gradients across the field, which would have the same effect as the intrinsic zodiacal light gradient. We model spatial gradients in F^q as a constant plus linear function of the x and y coordinates. The choice of the coordinate system is irrelevant, as the coefficients will simply adjust appropriately for any chosen system.

A.4. Exponential Decay

The final systematic effect evident in F^q is an apparent decaying response (with a negative amplitude) across each AOR. This trend can be fit by a simple exponential decay as a function of frame number in each AOR. However, there are both fast and slow decay terms with e -folding constants of 9 and 70 frames. We model this decay as a linear combination of these two exponential decays. This effect was also noted by Krick et al. (2011), but it appears more cleanly here.

The net model for the temporal variation in F^q is thus given by

$$\begin{aligned}
 F_{\text{model}}^q = & A \text{ ZODY_EST} + B_1 \text{ FRAMEDLY} \\
 & + B_2 \text{ FRAMEDLY}^2 + B_3 \text{ FRAMEDLY}^3 \\
 & + C + D_x x + D_y y + E_9 e^{-\text{frame}/9} \\
 & + E_{70} e^{-\text{frame}/70}.
 \end{aligned} \tag{4}$$

Figure 10 shows the residual F^q after successive subtraction of each of the components of F_{model}^q (with arbitrary offsets for clarity).

At $3.6\ \mu\text{m}$ the first-frame effect is responsible for most of the variance in F^q , as seen by comparing the derived F^q (black dots) with the derived F^q minus the fitted first-frame effect (red dots). At $4.5\ \mu\text{m}$, the zodiacal light trend is clearly dominant. Therefore, at $4.5\ \mu\text{m}$ the red dots represent the derived F^q minus the fitted zodiacal light trend.

The comparison of the red and orange dots in both panels shows the subsequent subtraction of the zodiacal light trend

($3.6\ \mu\text{m}$) and the first-frame effect ($4.5\ \mu\text{m}$). The zodiacal light trend has little effect at $3.6\ \mu\text{m}$. The influence of the first-frame effect is now clear at $4.5\ \mu\text{m}$, though far smaller in amplitude than at $3.6\ \mu\text{m}$.

Comparison between the orange and green dots shows the subsequent subtraction of the spatial gradient terms at both wavelengths. The AORs were designed such that the spatial gradients map into oscillations with a period of 24 frames. This makes them distinguishable from the slower monotonic change in the zodiacal light intensity, which occurs as a function of time. The amplitudes of the gradient terms are visibly larger in the earliest AOR and decrease across AORs as does the zodiacal light intensity.

The green dots clearly show the exponential decay behavior. At $3.6\ \mu\text{m}$, the slow 70-frame decay is evident in the first AORs, but there is a gradual transition to the faster nine-frame decay in the later AORs. At $4.5\ \mu\text{m}$, the amplitude of the decay is much smaller, and the slow 70-frame decay is dominant for all AORs.

After removal of the exponential decays, the blue dots show a fairly random distribution, with a standard deviation that is >10 times smaller than present in the original F^q . These residual dispersions of $\sigma = 4.7 \times 10^{-4}$ and 2.5×10^{-4} MJy sr $^{-1}$ represent an upper limit on the accuracy of the F^q term of the self-calibration. The residual variation may still be accounting for real effects in the data, but the specific nature of such effects has not been identified here.

APPENDIX B MODEL DEPTH

A critical aspect of this analysis is the use of a source model to remove the effects of (a) the emission of extended sources and point-spread function wings that project beyond the masked areas and (b) faint sources that cannot be masked without adversely decreasing the fraction of area available for analysis. Figure 11 shows power spectra of the masked images as the depth of the source model (i.e., the number of components subtracted) is linearly increased. Our choice is to use the model depth at which the skewness of the intensities of the unmasked pixel is zero. This assumes that

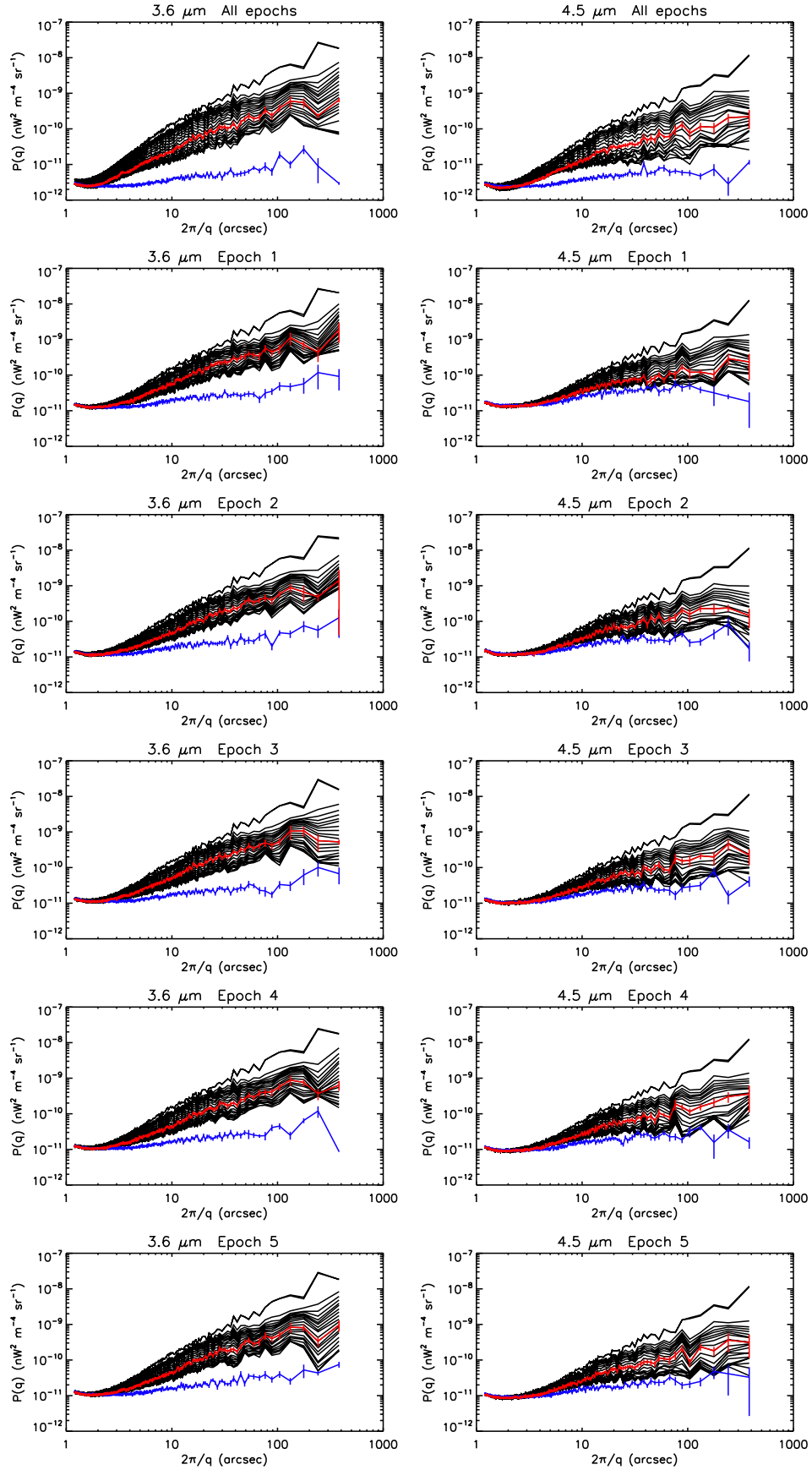


Figure 11. Power spectra shown at various model depths for the combined and separate epochs, at $3.6\ \mu\text{m}$ (left) and $4.5\ \mu\text{m}$ (right). The black lines show that the large-scale power does drop as the source model is pushed deeper. The red lines show the power spectra at “optimal” model depth when the skewness of the background (excluding outliers) is zero. The blue lines show the $A - B$ power spectra.

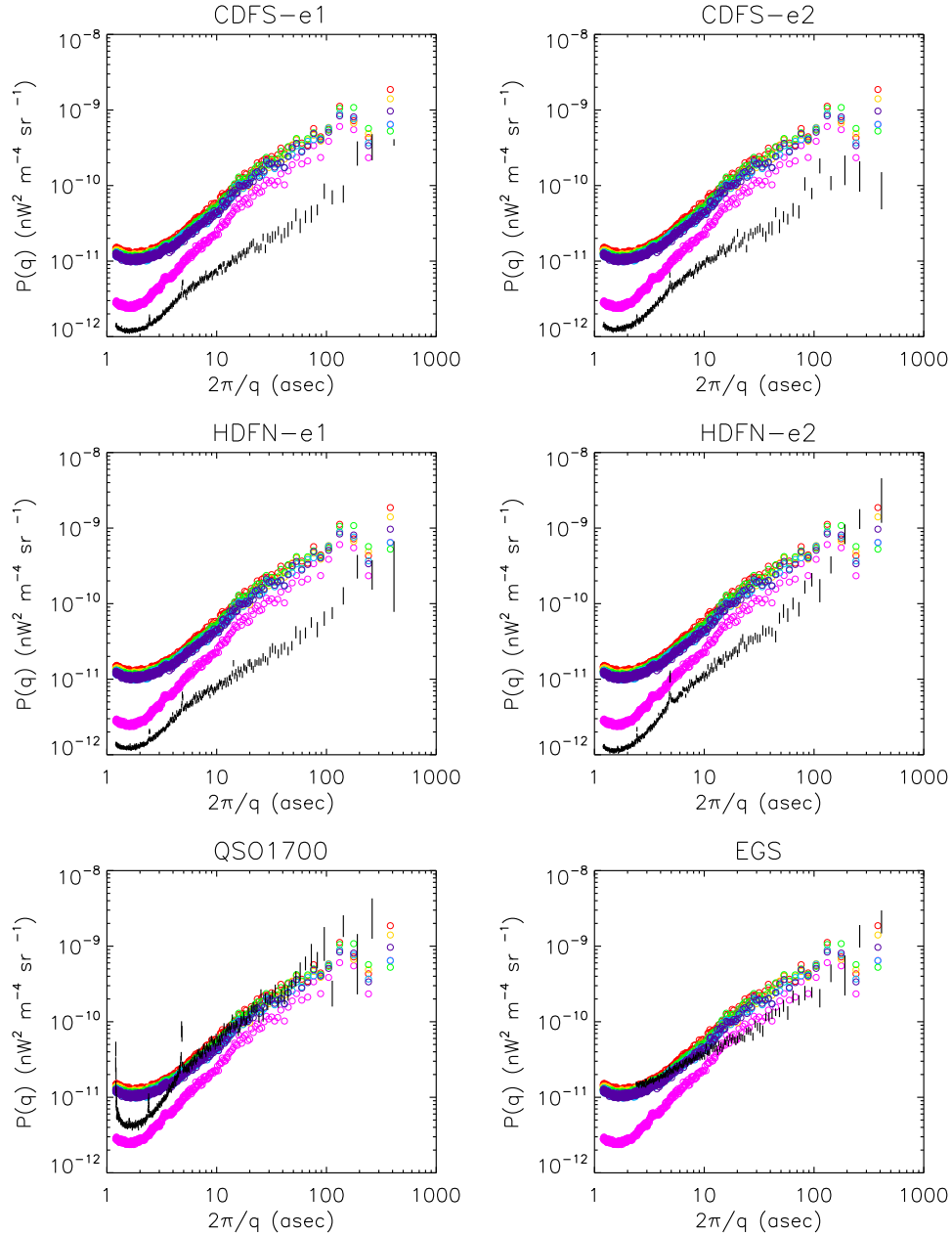


Figure 12. Comparison of the $3.6\ \mu\text{m}$ power spectra measured here (red, orange, green, blue, violet, and magenta: epochs 1–5, and all epochs combined) with the power spectra measured in six fields from Arendt et al. (2010) as indicated by the black error bars.

a positive skewness signifies the presence of residual sources in the image, and that a negative skewness indicates that the model has begun subtracting the positive side of the noise distribution rather than actual sources. The zero-skewness models are evaluated independently for each epoch and are indicated by red lines (with error bars) in Figure 11. The power spectra of the $A - B$ images are indicated by the blue lines. This figure is analogous to Figures 8–13 of Arendt et al. (2010).

APPENDIX C COMPARISON WITH PRIOR RESULTS

Figure 12 compares the power spectra measured here with those measured previously in Arendt et al. (2010). The

previous power spectra are indicated by the black error bars. The power spectra measured here for epochs 1–5 are rainbow colored from red to blue. Magenta symbols indicate all epochs combined. The smallest-scale power (dominated by white noise) decreases appropriately when all epochs are combined, whereas the large-scale power is not strongly reduced by combining epochs. The large-scale power is much higher than that seen in the deeper CDFS and HDFN observations, but is comparable to that of the shallower QSO1700 and EGS fields.

Figure 13 shows the same comparisons at $4.5\ \mu\text{m}$. In this case, the shot-noise level of the combined epochs is similar to that observed in the deep CDFS and HDFN fields. The large-scale power is also close to the levels measured in these deep fields.

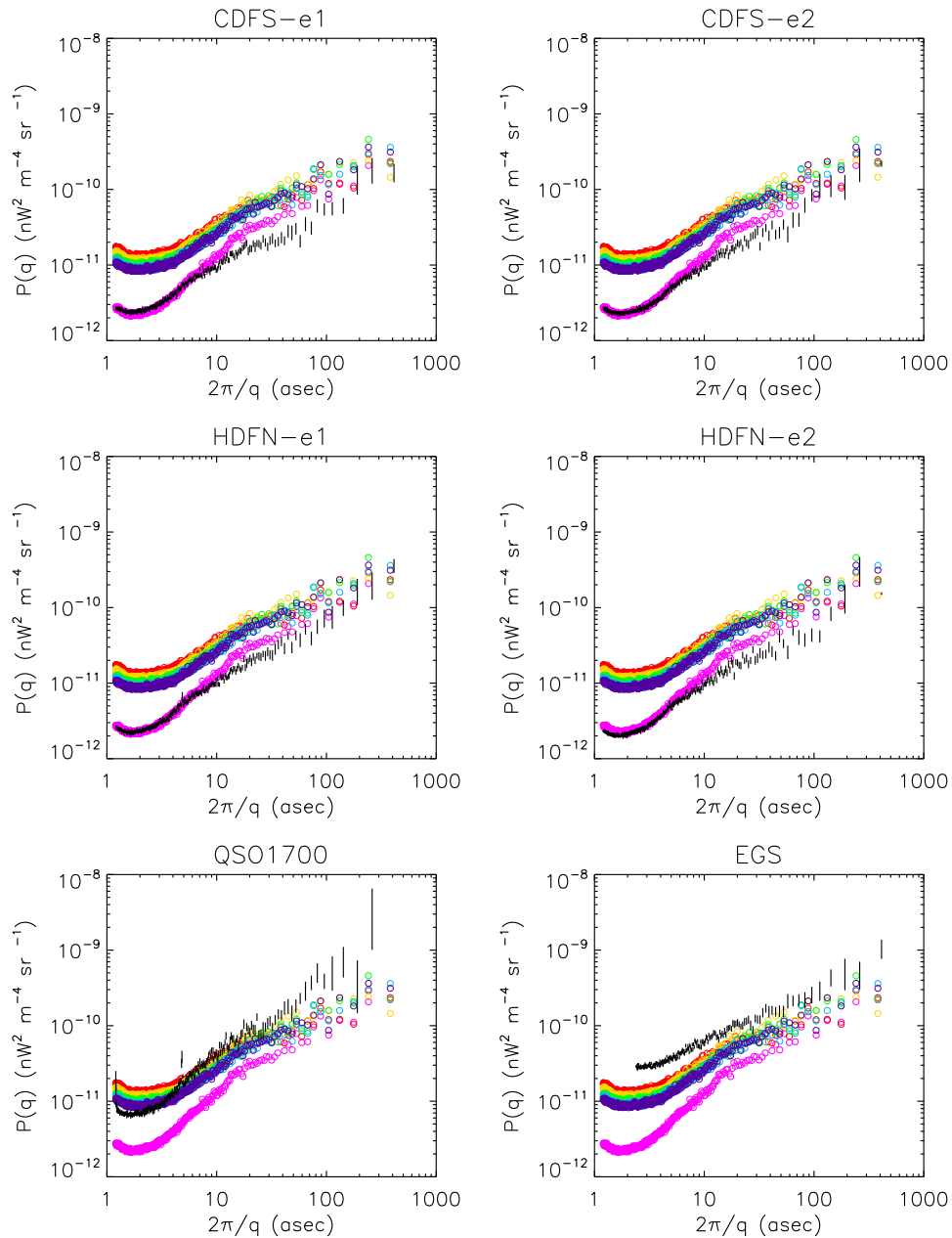


Figure 13. Same as Figure 12, but for 4.5 μm power spectra.

REFERENCES

- Abraham, P., Leinert, C., & Lemke, D. 1997, *A&A*, **328**, 702
- Arendt, R. G., Kashlinsky, A., Moseley, S. H., & Mather, J. 2010, *ApJS*, **186**, 10
- Arendt, R. G., Odegard, N., Weiland, J. L., et al. 1998, *ApJ*, **508**, 74
- Ashby, M. L. N., Willner, S. P., Fazio, G. G., et al. 2013, *ApJ*, **769**, 80
- Ashby, M. L. N., Willner, S. P., Fazio, G. G., et al. 2015, *ApJS*, **218**, 33
- Cooray, A., Smidt, J., de Bernardis, F., et al. 2012, *Natur*, **490**, 514
- Cooray, A., Sullivan, I., Chary, R.-R., et al. 2007, *ApJL*, **659**, L91
- Donnerstein, R. L. 2015, *MNRAS*, **449**, 1291
- Fazio, G. G., Hora, J. L., Allen, L. E., et al. 2004, *ApJS*, **154**, 10
- Fixsen, D. J., Moseley, S. H., & Arendt, R. G. 2000, *ApJS*, **128**, 651
- Gehrz, R. D., Roellig, T. L., Werner, M. W., et al. 2007, *RScI*, **78**, 011302
- Hauser, M. G., Arendt, R. G., Kelsall, T., et al. 1998, *ApJ*, **508**, 25
- Helgason, K., Ricotti, M., & Kashlinsky, A. 2012, *ApJ*, **752**, 113
- Kashlinsky, A., Arendt, R. G., Ashby, M. L. N., et al. 2012, *ApJ*, **753**, 63
- Kashlinsky, A., Arendt, R. G., Mather, J., & Moseley, S. H. 2005, *Natur*, **438**, 45
- Kashlinsky, A., Arendt, R. G., Mather, J., & Moseley, S. H. 2007a, *ApJL*, **654**, L1
- Kashlinsky, A., Arendt, R. G., Mather, J., & Moseley, S. H. 2007b, *ApJL*, **654**, L5
- Kashlinsky, A., Mather, J. C., & Odenwald, S. 1996a, *ApJL*, **473**, L9
- Kashlinsky, A., Mather, J. C., Odenwald, S., & Hauser, M. G. 1996b, *ApJ*, **470**, 681
- Kashlinsky, A., & Odenwald, S. 2000, *ApJ*, **528**, 74
- Kashlinsky, A., Odenwald, S., Mather, J., Skrutskie, M. F., & Cutri, R. M. 2002, *ApJL*, **579**, L53
- Kelsall, T., Weiland, J. L., Franz, B. A., et al. 1998, *ApJ*, **508**, 44
- Krick, J. E., Bridge, C., Desai, V., et al. 2011, *ApJ*, **735**, 76
- Krick, J. E., Glaccum, W. J., Carey, S. J., et al. 2012, *ApJ*, **754**, 53
- Landsman, W. B. 1993, in *ASP Conf. Ser. 52, Astronomical Data Analysis Software and Systems II*, ed. R. J. Hanisch, R. J. V. Brissenden, & J. Barnes (San Francisco, CA: ASP), 246
- Matsumoto, T., Kim, M. G., Pyo, J., & Tsumura, K. 2015, *ApJ*, **807**, 57
- Matsumoto, T., Matsuura, S., Murakami, H., et al. 2005, *ApJ*, **626**, 31
- Matsumoto, T., Seo, H. J., Jeong, W.-S., et al. 2011, *ApJ*, **742**, 124
- Matsuura, M., Dwek, E., Meixner, M., et al. 2011, *Sci*, **333**, 1258

- Mitchell-Wynne, K., Cooray, A., Gong, Y., et al. 2015, [NatCo](#), **6**, 7945
- Odenwald, S., Kashlinsky, A., Mather, J. C., Skrutskie, M. F., & Cutri, R. M. 2003, [ApJ](#), **583**, 535
- Pyo, J., Matsumoto, T., Jeong, W.-S., & Matsuura, S. 2012, [ApJ](#), **760**, 102
- Scoville, N., Aussel, H., Brusa, M., et al. 2007, [ApJS](#), **172**, 1
- Seo, H. J., Lee, H. M., Matsumoto, T., et al. 2015, [ApJ](#), **807**, 140
- Sullivan, I., Cooray, A., Chary, R.-R., et al. 2007, [ApJ](#), **657**, 37
- Thompson, R. I., Eisenstein, D., Fan, X., Rieke, M., & Kennicutt, R. C. 2007a, [ApJ](#), **657**, 669
- Thompson, R. I., Eisenstein, D., Fan, X., Rieke, M., & Kennicutt, R. C. 2007b, [ApJ](#), **666**, 658
- Werner, M. W., Roellig, T. L., Low, F. J., et al. 2004, [ApJS](#), **154**, 1
- Zemcov, M., Smidt, J., Arai, T., et al. 2014, [Sci](#), **346**, 732